Tractor Propeller-Pylon Interaction, Part II: Mitigation of Unsteady Pylon Loading by Application of Leading-Edge Porosity

della Corte, B.; Sinnige, Tomas; de Vries, Reynard; Avallone, Francesco; Ragni, Daniele; Eitelberg, Georg; Veldhuis, Leo

DOI
10.2514/6.2017-1176

Publication date
2017

Document Version
Accepted author manuscript

Published in
55th AIAA Aerospace Sciences Meeting

Tractor Propeller–Pylon Interaction, Part II: Mitigation of Unsteady Pylon Loading by Application of Leading-Edge Porosity

B. Della Corte*

University of Naples Federico II, Naples, 80138, Italy

T. Sinnige†, R. de Vries‡, F. Avallone§, D. Ragni¶,
G. Eitelberg‖, and L. L. M. Veldhuis**

Delft University of Technology, Delft, 2629 HS, The Netherlands

Structure-borne noise can be a relevant source of cabin noise in advanced aircraft configurations with pylon-mounted tractor propellers. The periodic impingement of the propeller slipstream on the pylon causes unsteady loading that can be mitigated by applying passive porosity at the leading edge of the pylon. Pressure reconstruction from particle-image velocimetry was used to extract the unsteady pressure field around the pylon and the associated aerodynamic loads. Experimental results showed that porosity locally modifies the pylon near-wall pressure distribution because of the crossflow through the porous surface. Application of a porous leading edge reduced the intensity of the unsteady pressure fluctuations in the tip-vortex impingement region by approximately 5% and 30% on the suction and pressure sides of the pylon, respectively. Consequently, the unsteady pylon loading induced by the propeller tip vortices was reduced by 25%, thus resulting in a less intense source of vibrations. On the other hand, pylon drag was locally increased. Based on the experimental data, projections of the drag penalty were made for a generic pylon design. The resulting pylon drag penalty equaled 15% up to 35% for angles of attack of 0° up to 9°. This drag penalty was attributed to the early onset of transition caused by the increased surface roughness of the porous insert, and viscous dissipation of the crossflow through the cavity of the porous insert.

I. Introduction

Propeller propulsion has gained renewed interest because of low thrust specific fuel consumption and the stricter regulations to reduce fuel burn for civil transport aircraft.[1] However, the increased propulsive efficiency comes with a larger intensity of ambient and in-cabin noise when compared to an equivalent jet aircraft. Aft-fuselage engine configurations lead to reduced in-cabin noise levels by placing the propeller plane away from the cabin. Both pusher and tractor layouts have been studied, each having specific benefits and drawbacks.[2,3] An advantage of the pylon-mounted tractor configuration is the elimination of the noise noise generated by the pylon-wake impingement on the propeller blades occurring for pusher propellers.[4,5] However, the tractor layout suffers from *structure-borne* noise, caused by pylon vibrations excited by the interaction between the propeller slipstream and the airframe. Previous studies have shown that this source of noise can be relevant to in-cabin noise compared to direct propeller noise.[6,7] The largest pressure fluctuations and unsteady loads are generated by the propeller blade's tip vortex impinging on the pylon.[8] As a consequence, alleviation of this interaction may be effective to reduce the associated structure-borne noise.

*M. Sc. Student, Fac. of Aerospace Eng., Bia.DellaCorte@studenti.unina.it.
†Ph. D. Candidate, Flight Performance and Propulsion Section, Fac. of Aerospace Eng., T.Sinnige@tudelft.nl, AIAA member.
‡M. Sc. Student, Flight Performance and Propulsion Section, Fac. of Aerospace Eng.
§Postdoctoral Researcher, Aeroacoustics Section, Fac. of Aerospace Eng., F.Avallone@tudelft.nl, AIAA member.
¶Assistant Professor, Aeroacoustics Section, Fac. of Aerospace Eng., D.Ragni@tudelft.nl, AIAA member.
‖Full Professor, Flight Performance and Propulsion Section, Fac. of Aerospace Eng., AIAA member.
**Full Professor, Head of Flight Performance and Propulsion Section, Fac. of Aerospace Eng., AIAA member.

An example porous layout is schematically represented in Fig. 1. It consists of an outer porous surface and an inner solid surface with the same shape. An inner cavity or plenum is present between the two surfaces. In presence of a pressure gradient, there is crossflow through the porous surface from high to low pressure regions. This feature of porous surfaces has been demonstrated in various scientific communications.[12–16] Previous computational studies on rotor–stator interactions have shown that the application of passive porosity could significantly alleviate the intensity of the unsteady loads due to wake-impingement phenomena.[9,10] Moreover, reductions of the unsteady pressure fluctuations caused by blade–vortex interactions have been demonstrated.[11]

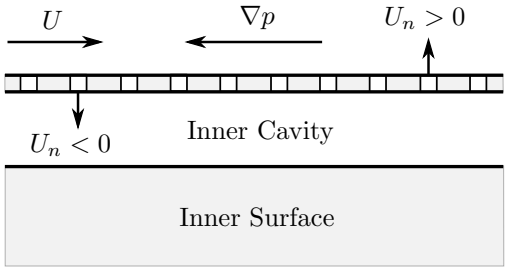

Figure 1. Main features of passive porosity.

The experimental study described in this paper aims at investigating the effectiveness of the application of passive porosity at the leading edge of a pylon as a passive strategy to mitigate unsteady pylon loads in a pylon-mounted tractor-propeller configuration. A baseline solid pylon and two porous configurations with different hole diameters were tested. Particle-image velocimetry (PIV) was used to characterize the unsteady three-dimensional flow past the pylon in the slipstream-impingement region. Moreover, the steady aerodynamic performance of the pylon was measured for a range of angles of attack to quantify the change in lift and drag caused by the porous leading edge.

II. Methodology

II.A. Wind-Tunnel Facility and Models

Measurements were carried out in the Low-Turbulence Wind Tunnel (LTT) at Delft University of Technology. The wind tunnel has a closed test section which measures 1.8 m in width, 1.2 m in height, and 2.6 m in length and operates up to 120 m/s. The freestream turbulence is below 0.1% at a freestream velocity of 40 m/s.

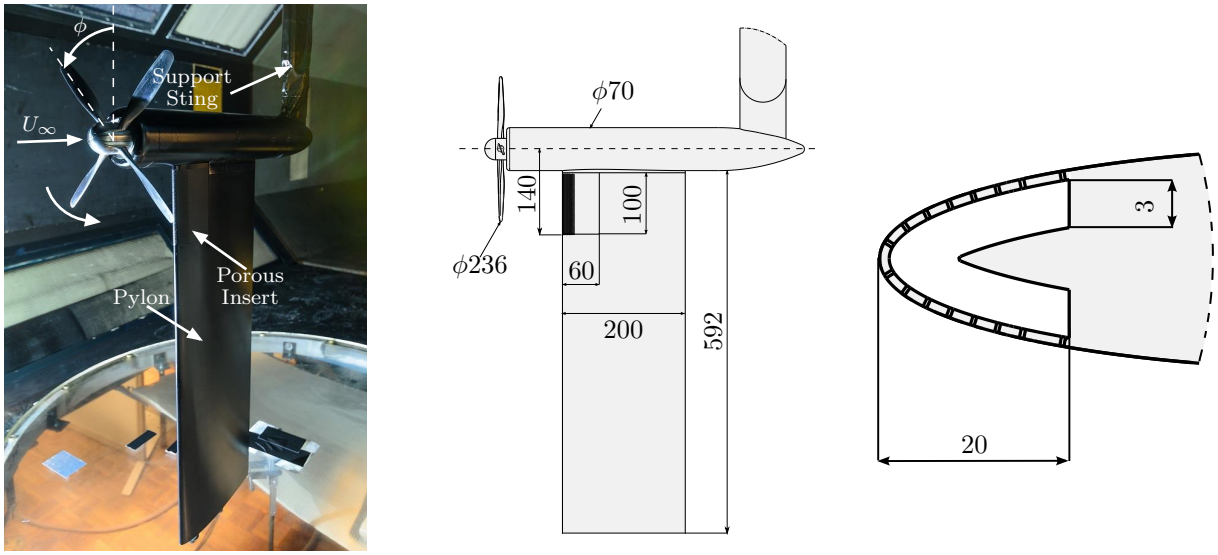

(a) Picture of the setup. (b) Side view of the model. (c) Section of the porous insert.

Figure 2. Experimental setup with the porous insert with hole diameter of 0.5 mm installed at the leading edge of the pylon. Dimensions are in millimeters.

The experimental setup is shown in Fig. 2. The 4-bladed propeller model had a diameter ($2R$) of 236 mm and was mounted on a nacelle supported by a sting fixed to the ceiling of the test section. The blade pitch angle at 75% of the radius was set to 23°. The pylon model, positioned vertically on the lower side of the nacelle, consisted of an unswept, untapered wing. The pylon was shaped as a NACA 0012 airfoil with chord of 200 mm. The span of 592 mm was selected to fill the vertical spacing between the nacelle and the floor of the test section. The pylon model was equipped with an interchangeable leading edge in the spanwise

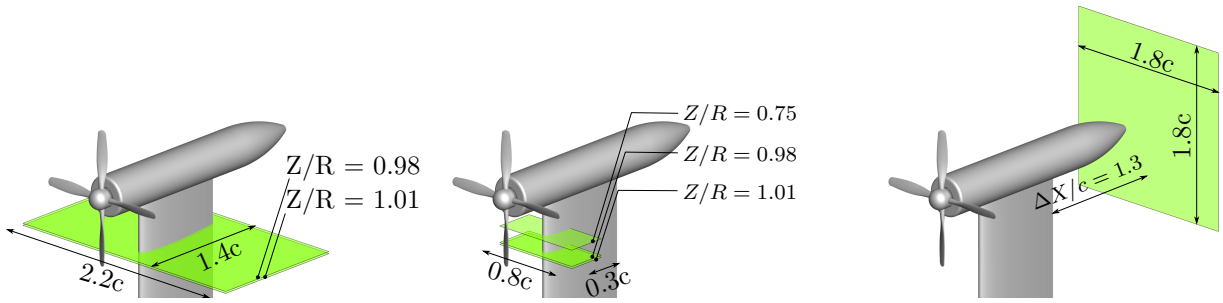

(a) Stereoscopic PIV on the large fields of view (LFOV).

(b) Planar PIV on the leading edge field of view (LEFOV).

(c) Stereoscopic PIV on the wake field of view (WFOV).

Figure 3. Schematic indicating the size and locations of PIV measurement planes.

region of the pylon washed by the propeller slipstream. A baseline solid insert and two different porous leading-edge inserts were tested. The two porous leading edges were made by a surface with a perforated skin, with hole diameters of 0.5 mm and 1.0 mm, respectively. The depth of the plenum below the perforated surface was equal to 3 mm, as shown in Fig. 2c. The porosity factor σ, defined as the ratio between the open surface and the total surface, and the chordwise extent of the porous patch were selected based on the optimal configuration identified by Tinetti et al.[9,10,17,18] The porous patch extended from the leading edge up to 10% chord. The porosity distribution followed a constant value of 0.22 for $0 < X/c < 0.05$, after which the porosity decreased elliptically down to 0.10 for $0.05 < X/c < 0.10$, with X the chordwise position from the leading edge and c the pylon chord.

II.B. Measurement Techniques

The aerodynamic effects of the application of the porous insert at the leading edge of the pylon were quantitatively assessed using particle-image velocimetry. Three different PIV setups were used. Figure 3 shows the size and position of the corresponding measurement domains relative to the models.

The flowfields around the pylon models were measured using two different PIV setups (Fig. 3). Phase-locked stereoscopic PIV measurements were carried out in large fields of view (LFOV) on the two sides of the pylon, as shown in Fig. 3a. The PIV measurement setup was vertically traversed to measure at two different spanwise positions. Moreover, phase-locked planar PIV measurements were taken in smaller fields of view around the leading edge (LEFOV) to achieve higher spatial resolution, as sketched in Fig. 3b. The PIV plane was traversed vertically to measure at three different locations along the pylon span. Finally, the effects of the porous insert on the aerodynamic performance of the pylon were assessed using stereoscopic PIV and wake-rake measurements in a plane perpendicular to the flow, positioned in the wake of the model (WFOV), see Fig. 3c.

For all the PIV measurements, seeding was provided by a SAFEX Twin Fog generator with SAFEX Inside Nebelfluid, a mixture of diethylene-glycol and water. The particle tracers had an average diameter and relaxation time of the order of 1 µm and 1 µs, respectively. Illumination was provided by Quantel Evergreen and/or Quantel Twin BSL lasers (Nd:YAG, 200 mJ/pulse), depending on the PIV setup. For the LEFOV setup, the two lasers were used simultaneously to illuminate both sides of the pylon. Two LaVision Imager Pro LX 16Mpixel cameras (4872 × 3248 pixel, pixel size of 7.4 µm) were used for the LEFOV and WFOV setups, while four cameras were used for the LFOV setup. LaVision Davis 8 software was used for acquisition and post-processing. Imaging and PIV details for all three setups are reported in Table 1.

II.C. Test Cases

The freestream velocity U_∞ was set to 40 m/s for all measurements. The propeller operating point was selected after measurements of the isolated propeller performance.[19] The thrust setting was chosen such that the propeller operated in the linear part of the thrust curve, thereby avoiding separation on the blades. This corresponded to an advance ratio of $J = U_\infty/nD = 0.8$ and a thrust coefficient $C_T = T\rho_\infty^{-1}n^{-2}D^{-4}$ of 0.095. The Reynolds number based on the pylon chord Re_c was approximately 5.5×10^5. The pylon angle of attack α was set to 0° for most of the test cases and then switched to −6°, 3°, 6° and 9° for wake measurements in the WFOV.

Table 1. Imaging and PIV details

Imaging and PIV parameters	LFOV	LEFOV	WFOV
Camera setup	Stereoscopic	Planar	Stereoscopic
Focal length (mm)	200	200	105
Digital resolution (pixel/mm)	16	50	12
Field of view (mm^2)	280×450	60×160	350×350
Freestream particle displacement (pixel)	12	10	13
Pulse delay (μs)	19	5	40
Final interrogation window (pixel^2)	48×48	24×24	32×32
Overlap factor	50%	50%	50%
Spatial resolution (mm)	1.58	0.22	1.95
Number of images[a]	250/300	300/500	-/500
Number of cameras	4	2	2
Number of lasers	1	2	1
Acquisition rate (Hz)	0.55	0.78	0.78

[a]Phase-locked/phase-uncorrelated measurements.

II.D. Data Post-Processing

II.D.1. PIV-based Pressure and Lift Computation

The in-plane pressure field was inferred from the PIV velocity data on the LFOV and LEFOV (Fig. 3a and 3b) by solving the Poisson pressure equation obtained from the incompressible Navier–Stokes equations.[20–22] Temporal and spatial derivatives were computed with three-point central schemes. The Poisson equation was solved using a second-order scheme following Ragni et al.[23] Finally, PIV velocity and pressure data on the LFOV were combined to obtain the pylon sectional lift in the PIV measurement planes following a contour-integration approach.[24–27]

Phase-locked multi-plane stereoscopic PIV measurements on the LFOV allowed a full characterization of the three-dimensional flow at the tip-vortex impingement position. In contrast, the planar PIV measurements on the LEFOV did not allow measurements of the spatial and temporal derivatives of the out-of-plane component. However, previous studies have shown that in flowfields with a dominant flow direction, the out-of-plane motion does not strongly affect the estimation of the pressure if a global solution approach is used.[28,29] Near-wall surface-pressure data were extracted at 1.5 mm and 12 mm away from the airfoil surface for the LEFOV and LFOV PIV data, respectively. This guarantees high signal-to-noise ratio in the estimation of the spatial and temporal derivatives.

The accuracy of the pressure computations was assessed following a Monte Carlo approach with 100 iterations. The magnitude of the random noise was set equal to the uncertainty of the PIV data. The resulting 95% confidence interval was assessed to be below 0.03. The uncertainty on the estimation of the lift coefficient was assessed by taking into account that the computed force should be invariant with the domain size. Therefore, the domain size was varied from 35% to 70% of the chord in 25 steps. The lift coefficient was then computed for the different domain sizes. The resulting 95% confidence interval was assessed to be below 0.003.

II.D.2. Wake Analysis

A quantitative wake analysis[30–33] was carried out to measure the effect of the porous leading edges on the steady aerodynamic forces acting on the pylon for a range of pylon angles of attack. Measurements were carried out with the propeller blades installed (propeller-on) and removed (propeller-off). Only the propeller-off cases are discussed in this paper.

The drag distribution on the pylon was computed by computing the change in the streamwise component of the momentum. The formulation of the problem allowed separate identification of the section profile drag coefficient c_{d_p} and the induced or vortex drag coefficient c_{d_i}. The lift distribution on the pylon was computed by use of the momentum balance with velocity inputs from PIV. Measurements were taken without the pylon to provide the necessary boundary conditions to compute the lift.

III. Results

Figure 4 schematically represents the tip-vortex impingement process on the pylon. Only one vortex filament is shown for clarity. For the given rotation direction, the side of the pylon at $Y < 0$ is referred to as the pressure side, while the side at $Y > 0$ is denoted the suction side. At the leading edge, the vortex filament bends and is subsequently split into two vortex filaments, which convect downstream along the two sides of the pylon. These vortices show spanwise displacements which are due to the changes in lift and vorticity along the span of the pylon.[34,35] A more detailed discussion is presented in the companion paper.[19]

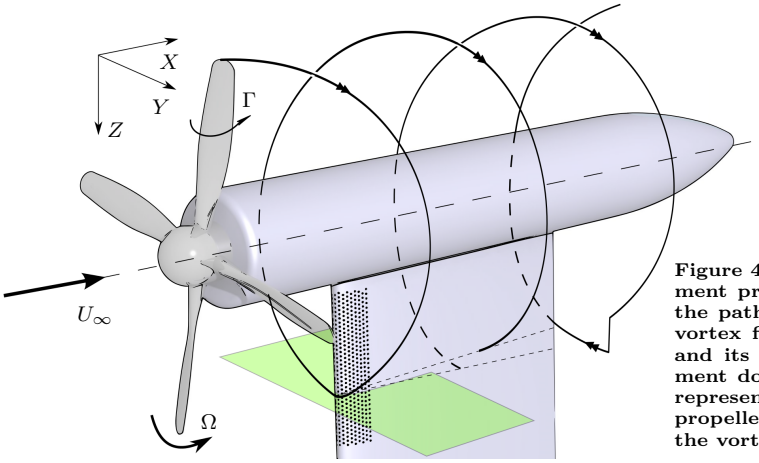

Figure 4. Schematic of the tip-vortex impingement process on the pylon. The sketch shows the path followed on the pylon surface by one vortex filament as it is convected downstream and its position with respect to the measurement domain at the leading edge (LEFOV). Ω represents the direction of the rotation of the propeller and Γ is the circulation. Note that the vortex helix is not drawn to scale.

Figures 5 and 6 show example velocity fields in the LFOV and LEFOV obtained for a fixed angular blade position ϕ. The angular position of the blade is defined positive in the direction of the propeller rotation and ϕ is set equal to 0° when the blade is positioned vertically on top. As can be seen in Fig. 5, the propeller tip vortex induces high velocity near the pylon surface. The vortex strength is higher on the pressure side because of the asymmetry induced by the propeller rotation in the measurement plane. Different considerations apply to the blade-wake impingement plane, which is the closest plane to the nacelle in Fig. 6. In this plane, the velocity is higher in the inner part of the domain because of the larger axial velocity in the propeller slipstream. The local slipstream is not as wide as the propeller disk since the measurement plane was below the propeller axis. The tip-vortex filament crosses this plane at a distance from the pylon surface and induces low velocity toward the edge of the measurement plane.

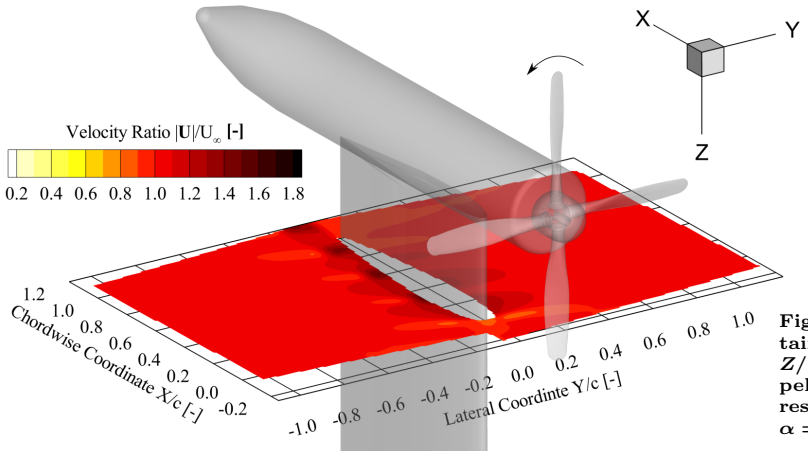

Figure 5. Flowfield obtained in the LFOV at $Z/R = 0.98$ from the propeller axis. Phase-locked results for $U_\infty = 40$ m/s, $\alpha = 0°$, $J = 0.8$ and $\phi = 90°$.

III.A. Time-Averaged Flowfield at the Pylon Leading Edge

Ensemble-averaging of uncorrelated flowfields was performed to map the time-averaged flow around the leading edge of the pylon. Figure 7 presents the phase-averaged velocity magnitude for the three pylon configurations and for both the blade-wake (Fig. 7a) and tip-vortex impingement positions (Fig. 7b). Figure 8 shows the near-wall pressure distributions obtained from these velocity fields.

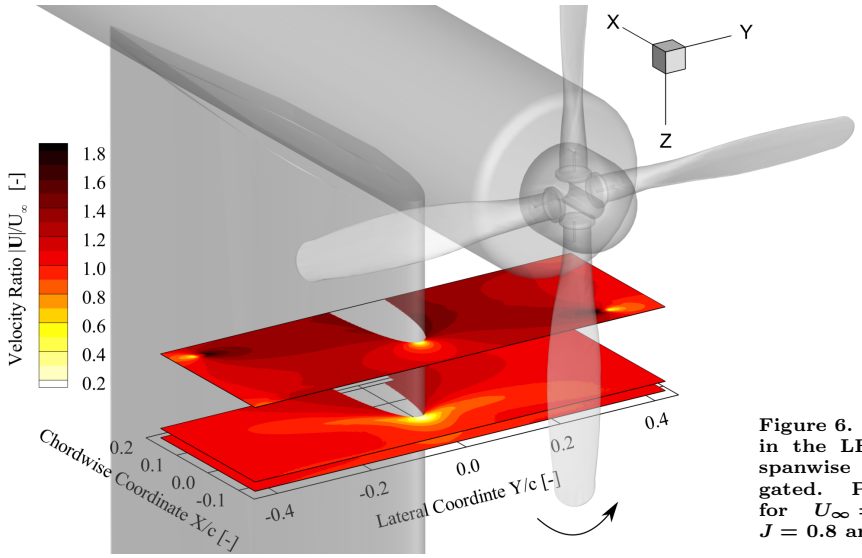

Figure 6. Flowfields obtained in the LEFOV at the three spanwise positions investigated. Phase-locked results for $U_\infty = 40\,\mathrm{m/s}$, $\alpha = 0°$, $J = 0.8$ and $\phi = 90°$.

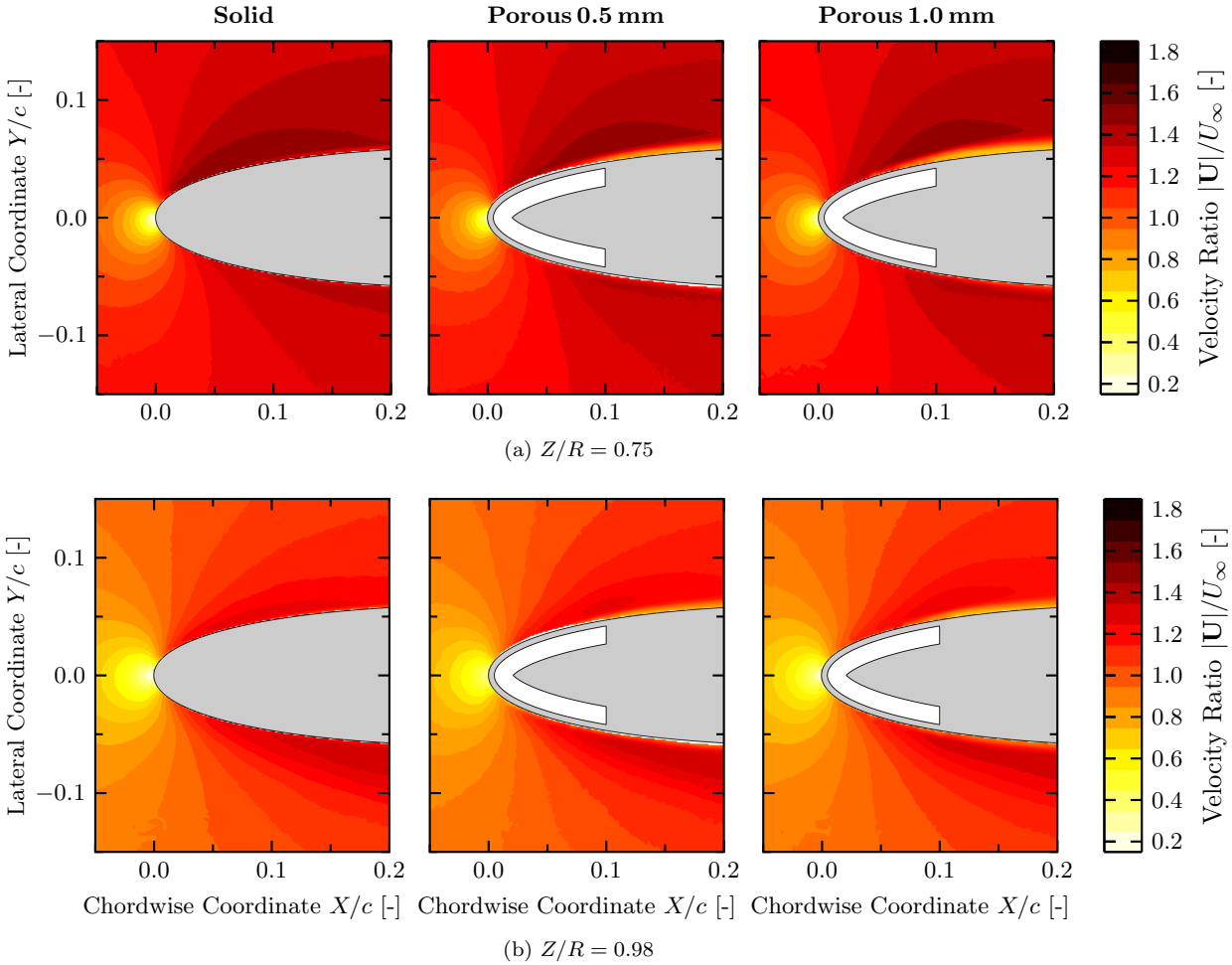

Figure 7. Velocity magnitude distributions in the blade-wake and tip-vortex impingement regions. Ensemble-averaged results for propeller-on, $U_\infty = 40\,\mathrm{m/s}$, $J = 0.8$ and $\alpha = 0°$.

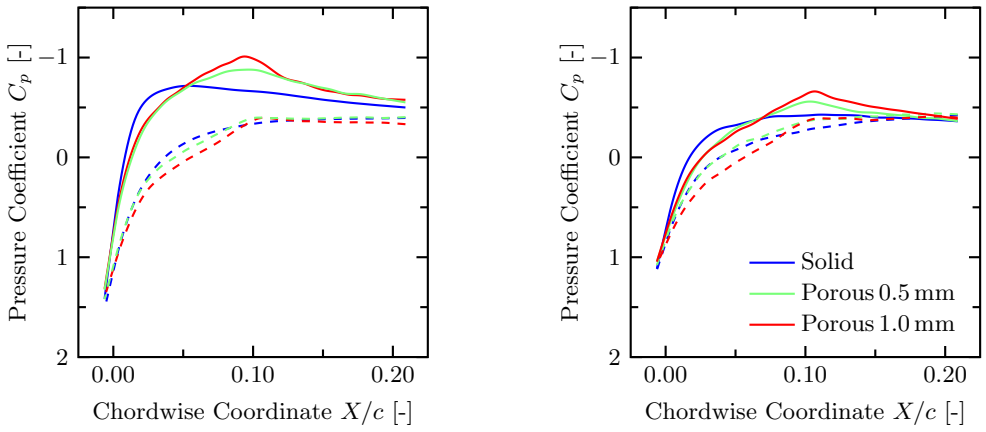

(a) $Z/R = 0.75$ (b) $Z/R = 0.98$

Figure 8. Pressure distributions at the pylon surface at different spanwise positions. Ensemble-averaged results for propeller-on, $U_\infty = 40$ m/s, $J = 0.8$ and $\alpha = 0°$. In the plots, solid lines refer to the suction side and dashed lines to the pressure one.

Comparing Fig. 7a and 7b, higher values of the velocity were measured at $Z/R = 0.75$ due to the acceleration induced across the propeller disk. Moreover, in the blade-wake impingement region (Fig. 7a) the swirl produced a visibly asymmetric flowfield. These effects can also be observed in the surface pressure distributions of Fig. 8, where at $Z/R = 0.75$ (Fig. 8a) the stagnation pressure and the pressure differential between the two sides of the pylon are higher compared to the lower plane (Fig. 8b).

The boundary-layer thickness increased by applying porosity in both the blade-wake and tip-vortex impingement regions, as visible in Fig. 7. The thicker boundary layer was caused by crossflow through the porous medium and by the onset of transition due to the increased surface roughness of the porous inserts. A thicker boundary layer was measured on the suction side of the airfoil due to the crossflow through the porous skin.

Figure 8 shows that the application of porosity strongly altered the surface pressure distribution. The crossflow through the porous medium altered the effective aerodynamic shape of the airfoil. As a result, the suction peak increased and displaced downstream. This effect was slightly dependent on the hole size and stronger on the Porous 1.0 mm pylon. On the porous pylons, the suction peak coincided with the end of the porous patch ($X/c = 0.10$). Similar changes to the surface pressure distribution are induced on a clean airfoil by increasing the thickness and/or displacing the location of maximum thickness toward the trailing edge.[36] This suggests that passive porosity affects the effective aerodynamic shape of the airfoil by changing the equivalent thickness distribution. These same conclusions were drawn by Mineck.[37] Similar features were also found in the combined experimental and numerical results obtained by Tinetti et al.[9,10,17] The downstream displacement of the suction peak was also found in the numerical work of Lee,[11] though in that particular study it was found that the suction peak decreased due to the application of porosity.

III.B. Unsteady Pylon Loading due to Tip-Vortex Impingement

Phase-locked velocity fields in the LEFOV at $Z/R = 0.98$ are plotted in Fig. 9 for two different blade phase angles corresponding to the tip-vortex impingement.

Figure 9 shows that at $\phi = 97.5°$ (Fig. 9a) the vortex filament was almost tangent to the measurement plane and bent around the leading edge of the pylon. It progressively split into two vortex filaments along the two sides of the pylon. At $\phi = 120°$ (Fig. 9b), the vortex core crossed the measurement plane at $X/c \approx 0.12$. The vortex increased the velocity near the airfoil surface because of its position with respect to the measurement plane.

When the vortex core impinged at the pylon leading edge (Fig. 9a), a lower velocity was measured near the stagnation point of the solid pylon when compared with the two porous configurations. This is due to the fact that the porous surface allows crossflow through the inner cavity. At $\phi = 120°$ (Fig. 9b), the changes induced by porosity are more evident. Comparing the plots in Fig. 9b, the high velocity region induced locally by the tip vortex was displaced away from the pylon surface for the porous configurations. This is most likely due to both the crossflow though the porous inserts and the thicker turbulent boundary layer discussed above.

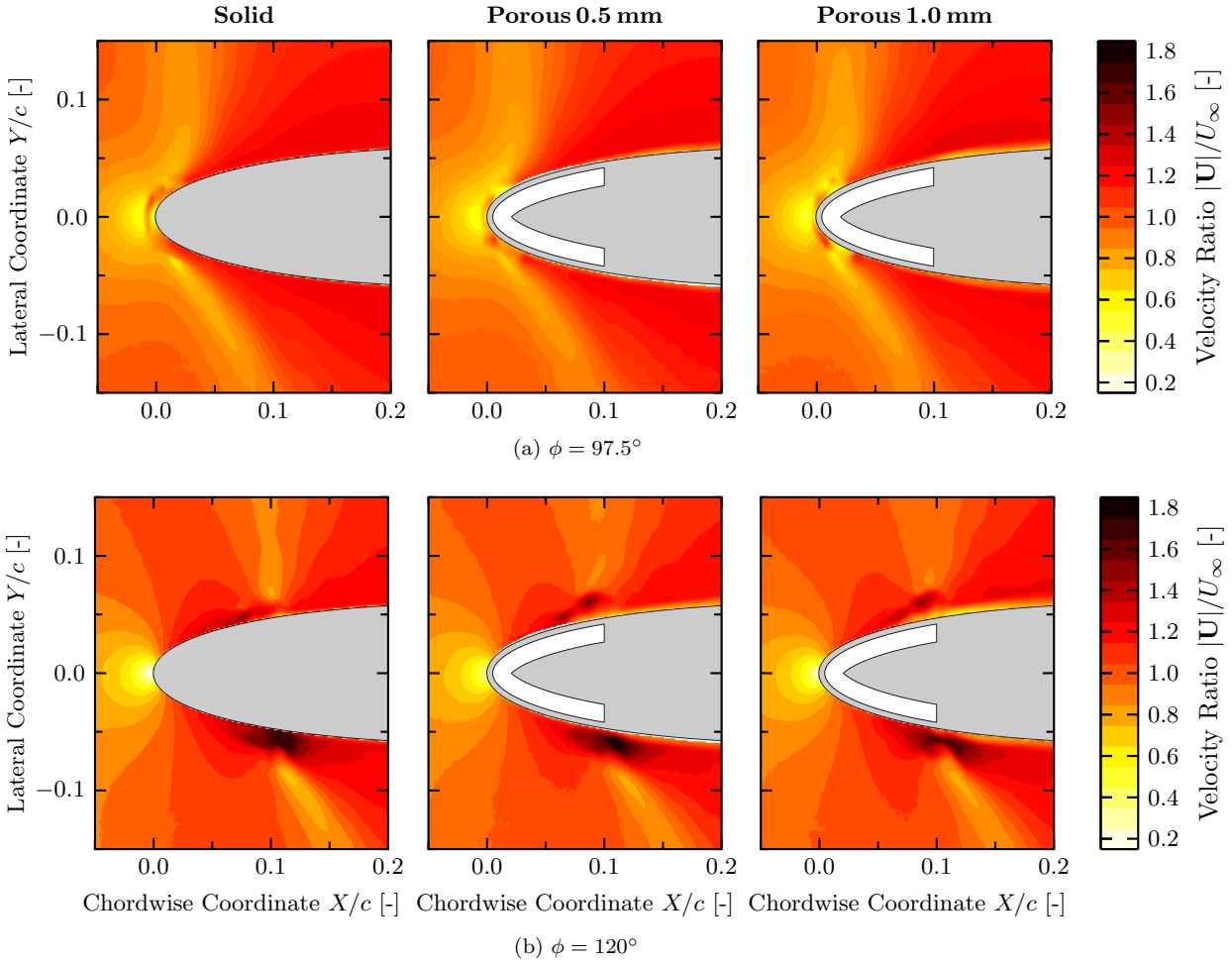

Figure 9. Velocity magnitude distributions in the tip-vortex impingement region at $Z/R = 0.98$ from the propeller axis. Phase-locked results for propeller-on, $U_\infty = 40$ m/s, $J = 0.8$ and $\alpha = 0°$.

The phase-evolution of the near-wall pressure was extracted from the data measured in the LFOV. Figure 10 shows the unsteady pressure coefficient ($C_p'(X,\phi) \triangleq C_p(X,\phi) - C_p^{avg}(X)$) at two chordwise locations at $Z/R = 0.98$. Since the vortex filament was above the measurement plane, it induced a velocity component in the opposite direction with respect to the main flow. Consequently, the vortex passage corresponds to the positive pressure peaks in Fig. 10.

From Fig. 10 it can be seen that the largest pressure fluctuations caused by the vortex impingement were measured on the suction side. The intensity of the pressure fluctuations reduced in chordwise direction, as also reported in the companion study.[19] Application of porosity reduced the intensity of the pressure fluctuations by approximately 5% on the suction side and 30% on the pressure side with respect to the solid leading edge.

The reduction of the near-wall pressure fluctuations should reduce the unsteady pylon loads. To verify this, aerodynamic loads were computed as described in Subsection II.D.1. The results are presented in Fig. 11, which shows the phase-varying sectional lift coefficient, defined as $c_l' \triangleq c_l(\phi) - c_l^{\text{avg}}$, for the solid pylon and the porous configuration with 1.0 mm hole diameter.

Figure 11 shows that the pylon lift increased as the vortex approached the leading edge, and a peak was measured at approximately $\phi = 52°$, when the tip vortex split into two vortex filaments. The application of porosity reduced the average lift coefficient bu approximately 35%, while the peak-to-peak amplitude of the lift fluctuations was decreased by approximately 25%. This confirms that the porous material reduced the unsteady pylon loading. The reduction of the average lift coefficient is consistent with the results measured in steady conditions (propeller-off, see Section III.C) and was likely due to a slight misalignment during the tests.

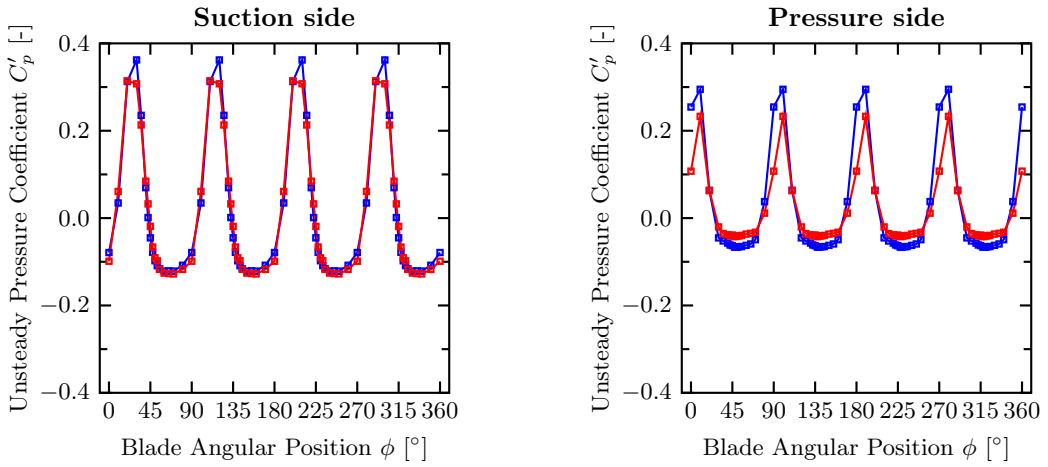

(a) $X/c = 0.05$

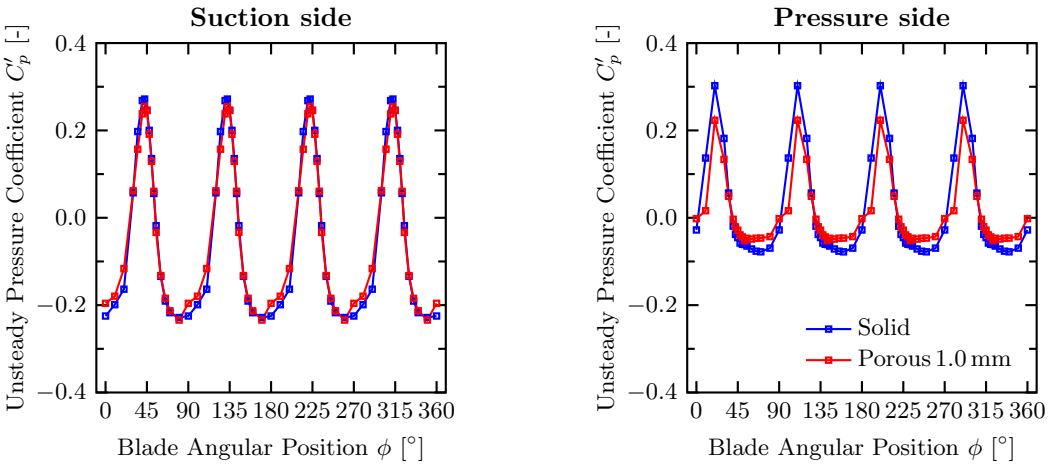

(b) $X/c = 0.10$

Figure 10. Unsteady pressure coefficient near the pylon surface at two different chordwise locations at $Z/R = 0.98$ from the propeller axis. Phase-locked results from the PIV on the LFOV for propeller on, $U_\infty = 40$ m/s, $J = 0.8$ and $\alpha = 0°$.

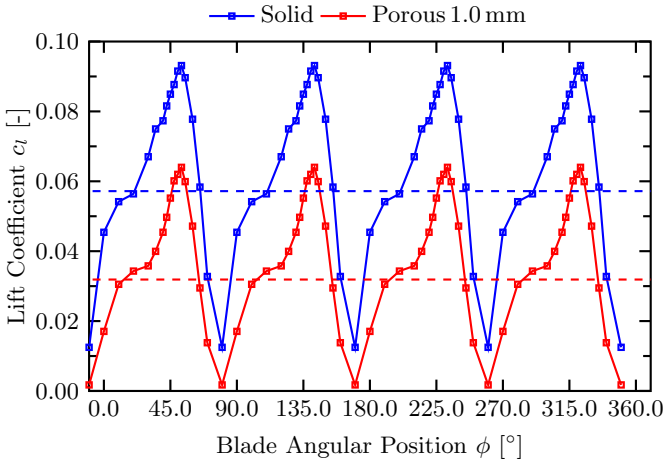

Figure 11. Unsteady sectional lift coefficient acting on two pylon configurations at the tip-vortex impingement position at $Z/R = 0.98$ from the propeller axis. Phase-locked measurements for propeller on, $U_\infty = 40$ m/s, $J = 0.8$ and $\alpha = 0°$. Average values of the lift coefficient indicated by the dashed lines.

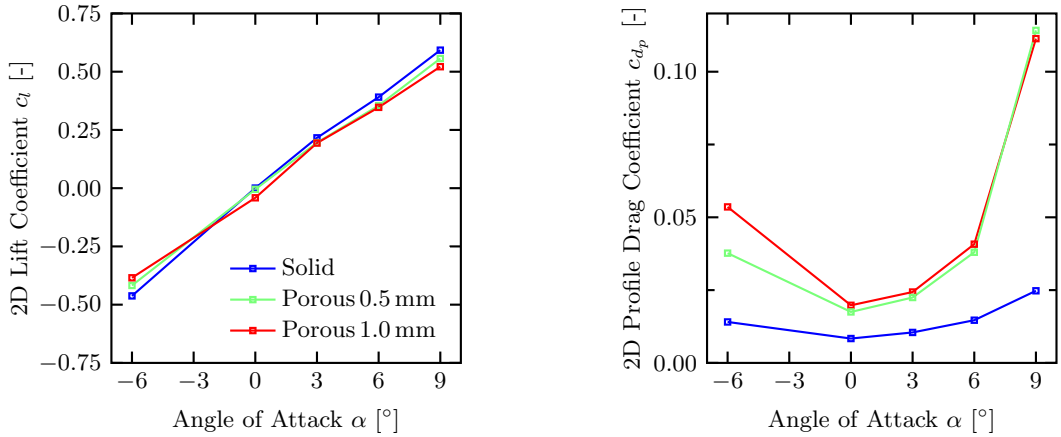

(a) Lift Coefficient

(b) Profile Drag Coefficient

Figure 12. Average sectional lift and drag coefficients on the three pylon configurations. Results for propeller-off, $U_\infty = 40\,\mathrm{m/s}$ and $Re_c = 5.5 \times 10^5$.

III.C. Propeller-Off Aerodynamic Performance

The aerodynamic performance of the porous leading-edge inserts was evaluated using a quantitative wake analysis. The resulting lift and drag polars are presented in Fig. 12 for the three pylon setups, while Table 2 summarizes the main results. As explained above, measurements were taken in the propeller-off configuration.

Table 2. Average sectional lift and drag coefficients on the three pylon configurations. Results for propeller-off, $U_\infty = 40\,\mathrm{m/s}$ and $Re_c = 5.5 \times 10^5$.

	Solid		Porous 0.5 mm		Porous 1.0 mm	
α°	c_l	c_{d_p}	c_l	c_{d_p}	c_l	c_{d_p}
−6	−0.46	0.014	−0.42	0.038	−0.38	0.054
0	0.00	0.008	0.00	0.018	−0.04	0.020
3	0.22	0.010	0.20	0.022	0.19	0.024
6	0.39	0.015	0.35	0.038	0.35	0.041
9	0.59	0.025	0.56	0.114	0.52	0.111

Figure 12a shows that the application of porosity did not significantly affect the lift generated locally by the pylon. Each pylon configuration displayed a c_l linearly increasing with α, though with a slope c_{l_α} which is lower than the value that would be expected for an isolated 2D NACA 0012.[36] The lower c_{l_α} is due to finite-wing effects. When set at incidence, the lift coefficient decreased by up to 12% and 9% for the Porous 1.0 mm and Porous 0.5 mm configurations with respect to the solid leading edge.

Figure 12b displays the profile drag coefficient c_{d_p} as a function of angle of attack. It is clear that the application of porosity increases the local c_{d_p}, with a penalty ranging from 125% to 350% for angles of attack varying between 0° and 9°. This increase in profile drag is mainly due to the viscous dissipation associated with the crossflow through the porous medium and the high surface roughness of the porous insert. No significant differences were found between the two porous configurations except at $\alpha = -6°$, where the Porous 1.0 mm pylon showed a 30% higher drag value. This discrepancy is probably due to an asymmetry in the Porous 1.0 mm model. These results demonstrate that the hole size does not have a significant influence on the aerodynamic performance of the pylon for the range of angles of attack investigated.

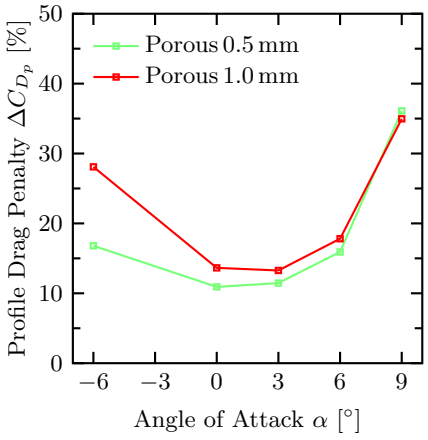

Figure 13. Projections of the profile drag penalty on a generic pylon configuration.

The sectional 2D profile drag penalty presented in Fig. 12b was used to make a projection of the drag penalty that would occur for a realistic pylon design treated with a porous leading edge placed only in the tip-vortex impingement region. A spanwise extent of the porous insert of 10% of the propeller diameter was selected, such that it only covered the region closest to the tip-vortex impingement position where the pressure fluctuations are the largest.[19] It was assumed that the effect of the porous material was limited to its spanwise extent on the pylon. Moreover, the pylon span was assumed equal to the propeller diameter to provide sufficient propeller tip-fuselage clearance. The resulting pylon drag penalties are plotted versus angle of attack in Fig. 13.

The predicted drag penalties shown in Fig. 12a amount to approximately 15% and 35% at the lowest and highest angle of attack considered. However, it should be noted that the low Reynolds number and freestream turbulence provided by the wind tunnel may have caused laminar flow over a large part of the surface of the solid pylon. In contrast, for the porous configurations the flow was turbulent because of the surface roughness of the porous insert and the crossflow through it. Under typical operating conditions, the higher Reynolds number would cause turbulent flow on a large extent of pylon surface, also for the solid pylon. This would lead to a reduced drag penalty due to the application of porosity.

IV. Conclusions & Outlook

The effectiveness of passive porosity in mitigating the unsteady pressures and loads caused by propeller-slipstream impingement on a pylon was experimentally assessed. Particle-image velocimetry was used to measure the flowfield around the pylon in the slipstream impingement region. Corresponding pressure fields and unsteady aerodynamic loading were obtained from the PIV data. Experimental results showed that the application of porosity at the leading edge of the pylon effectively modifies the near-wall surface pressure distribution. A reduction of unsteady pylon loads of 25% was achieved, promising benefits to in-cabin structure-borne noise. On the other hand, measurements showed that the porous leading edge increases locally the drag coefficient. Based on the experimental data, projections were made on a generic pylon design which showed a pylon drag penalty ranging from 15% to 35% by varying the angle of attack from 0° to 9°.

Currently, the effect of the hole size and cavity depth are under investigation. This will provide a more in-depth understanding of the changes to the flowfield caused by passive porosity and will aid in the definition of a more suitable design with minimized drag penalty.

References

[1]Dodds, W., "Engine and aircraft technologies to reduce emissions," ICCAIA Noise and Emissions Committee, San Diego, CA, USA, 2002.

[2]Page, M., Ivey, D., and Welge, H., "Ultra High Bypass Engine Applications to Commercial and Military Aircraft," SAE Technical Paper 861720, 1986.

[3]Goldsmith, I. M., "A study to define the research and technology requirements for advanced turbo/propfan transport aircraft," NASA Contractor Report 166138, 1981.

[4]Godston, J. and Reynolds, C., "Future prop-fans – Tractor or pusher," 21st AIAA, SAE, ASME, and ASEE, Joint Propulsion Conference, Monterey, CA, USA, 1985.

[5]Block, P. and Gentry Jr, C., "Directivity and Trends of Noise Generated by a Propeller in a Wake," NASA Technical Paper 2609, 1986.

[6]Cole III, J., Stokes, A. W., Garrelick, J., and Martini, K., "Analytical modeling of the structureborne noise path on a small twin-engine aircraft," NASA Contractor Report 18020, 1988.

[7]Eversman, W., Koval, L., and Ramakrishnan, J., "A comparison of the structureborne and airborne paths for propfan interior noise," University of Missouri, Mechanical and Aerospace Engineering Department, 1986.

[8]Miller, B. A., Dittmar, J. H., and Jeracki, R., "Propeller tip vortex – A possible contributor to aircraft cabin noise," *Journal of Aircraft*, Vol. 19, No. 1, 1982, pp. 84–86.

[9]Tinetti, A. F., Kelly, J. J., Bauer, S. X., and Thomas, R. H., "On the use of surface porosity to reduce unsteady lift," 15th AIAA Computational Fluid Dynamics Conference, Anaheim, CA, USA, 2001.

[10]Tinetti, A. F., Kelly, J. J., Thomas, R. H., and Bauer, S. X., "Reduction of Wake–Stator Interaction Noise Using Passive Porosity," 40th AIAA Aerospace Sciences Meeting and Exhibit, Reno, NV, USA, 2002.

[11]Lee, S., "Reduction of blade-vortex interaction noise through porous leading edge," *AIAA Journal*, Vol. 32, No. 3, 1994, pp. 480–488.

[12]Raghunathan, S., "Effect of porosity strength on passive shock-wave/boundary-layer control," *AIAA Journal*, Vol. 25, No. 5, 1987, pp. 757–758.

[13]Nagamatsu, H., Orozco, R., and Ling, D., "Porosity effect on supercritical airfoil drag reduction by shock wave/boundary layer control," 17th Fluid Dynamics, Plasma Dynamics, and Lasers Conference, Snowmass, CO, USA, 1984.

[14]Wood, R. M., Banks, D. W., and Bauer, S. X., "Assessment of passive porosity with free and fixed separation on a tangent ogive forebody," AIAA Atmospheric Flight Mechanics Conference, Hilton Head Island, SC, USA, 1992.

[15]Hunter, C. A., Viken, S. A., Wood, R. M., and Bauer, S. X., "Advanced aerodynamic design of passive porosity control effectors," 39th AIAA Aerospace Sciences Meeting and Exhibit, Reno, NV, USA, 2001.

[16]Khorrami, M. R. and Choudhari, M. M., "Application of passive porous treatment to slat trailing edge noise," NASA Technical Report 212416, 2003.

[17]Tinetti, A. F., *On the use of surface porosity to reduce wake-stator interaction noise*, Ph.D. thesis, Virginia Polytechnic Institute and State University, 2001.

[18]Frink, N. T., Bonhaus, D. L., Vatsa, V. N., S. Bauer, S. X., and Tinetti, A. F., "Boundary condition for simulation of flow over porous surfaces," *Journal of Aircraft*, Vol. 40, No. 4, 2003, pp. 692–698.

[19]de Vries, R., Sinnige, T., Della Corte, B., Avallone, F., Ragni, D., Eitelberg, G., and Veldhuis, L. L. M., "Tractor Propeller–Pylon Interaction, Part I: Characterization of Unsteady Pylon Loading," 55th AIAA Aerospace Sciences Meeting, Grapevine, TX, USA, 2017.

[20]van Oudheusden, B. W., "PIV-based pressure measurement," *Measurement Science and Technology*, Vol. 24, No. 3, 2013.

[21]Gurka, R., Liberzon, A., Hefetz, D., Rubinstein, D., and Shavit, U., "Computation of pressure distribution using PIV velocity data," 3rd International Workshop on Particle Image Velocimetry, Santa Barbara, CA, USA, 1999.

[22]Baur, T. and Köngeter, J., "PIV with high temporal resolution for the determination of local pressure reductions from coherent turbulence phenomena," 3rd International Workshop on Particle Image Velocimetry, Santa Barbara, CA, USA, 1999.

[23]Ragni, D., van Oudheusden, B. W., and Scarano, F., "3D pressure imaging of an aircraft propeller blade-tip flow by phase-locked stereoscopic PIV," *Experiments in Fluids*, Vol. 52, No. 2, 2012, pp. 463–477.

[24]Anderson Jr, J. D., *Fundamentals of aerodynamics*, McGraw-Hill, 2010.

[25]Kurtulus, D., Scarano, F., and David, L., "Unsteady aerodynamic forces estimation on a square cylinder by TR-PIV," *Experiments in Fluids*, Vol. 42, No. 2, 2007, pp. 185–196.

[26]van Oudheusden, B. W., Scarano, F., Roosenboom, E. W., Casimiri, E. W., and Souverein, L. J., "Evaluation of integral forces and pressure fields from planar velocimetry data for incompressible and compressible flows," *Experiments in Fluids*, Vol. 43, No. 2-3, 2007, pp. 153–162.

[27]Unal, M., Lin, J.-C., and Rockwell, D., "Force prediction by PIV imaging: a momentum-based approach," *Journal of Fluids and Structures*, Vol. 11, No. 8, 1997, pp. 965–971.

[28]De Kat, R. and van Oudheusden, B. W., "Instantaneous planar pressure determination from PIV in turbulent flow," *Experiments in Fluids*, Vol. 52, No. 5, 2012, pp. 1089–1106.

[29]Violato, D., Moore, P., and Scarano, F., "Lagrangian and Eulerian pressure field evaluation of rod-airfoil flow from time-resolved tomographic PIV," *Experiments in Fluids*, Vol. 50, No. 4, 2011, pp. 1057–1070.

[30]Veldhuis, L. and Rentema, D., "Quantitative wake surveys behind a tractor propeller-wing configuration," Aircraft Engineering, Technology, and Operations Congress, Los Angeles, CA, USA, 1995.

[31]Brune, G., "Quantitative low-speed wake surveys," *Journal of Aircraft*, Vol. 31, No. 2, 1994, pp. 249–255.

[32]Maskell, E., "Progress Towards a Method for the Measurement of the Components of the Drag of a Wing of Finite Span," Technical Report, Procurement Executive, Ministry of Defence, Royal Aircraft Establishment, RAE Farnborough, 1972.

[33]Betz, A., "A method for the direct determination of wing-section drag," NACA Technical Memorandum 337, 1925.

[34]Johnston, R. and Sullivan, J., "Unsteady wing surface pressures in the wake of a propeller," *Journal of Aircraft*, Vol. 30, No. 5, 1993, pp. 644–651.

[35]Thom, A. D., *Analysis of vortex-lifting surface interactions*, Ph.D. thesis, University of Glasgow, 2011.

[36]Abbott, I. H. and Von Doenhoff, A. E., *Theory of wing sections, including a summary of airfoil data*, Dover Publications, 1959.

[37]Mineck, R. E. and Hartwich, P. M., "Effect of full-chord porosity on aerodynamic characteristics of the NACA 0012 airfoil," NASA Technical Paper 3591, 1996.